The ROGDI protein mutated in Kohlschutter–Tonz syndrome is a novel subunit of the Rabconnectin-3 complex implicated in V-ATPase assembly

Received for publication, September 9, 2024, and in revised form, February 11, 2025 Published, Papers in Press, March 4, 2025,
https://doi.org/10.1016/j.jbc.2025.108381

Samuel R. Winkley and Patricia M. Kane*

From the Department of Biochemistry and Molecular Biology, SUNY Upstate Medical University, Syracuse, New York, USA

Reviewed by members of the JBC Editorial Board. Edited by Phyllis Hanson

V-ATPases are highly conserved ATP-driven rotary proton pumps found widely among eukaryotes that are composed of two subcomplexes: V_1 and V_0. V-ATPase activity is regulated in part through reversible disassembly, during which V_1 physically separates from V_0 and both subcomplexes become inactive. Reassociation of V_1 to V_0 reactivates the complex for ATP-driven proton pumping and organelle acidification. V-ATPase reassembly in *Saccharomyces cerevisiae* requires the RAVE complex (Rav1, Rav2, and Skp1), and higher eukaryotes, including humans, utilize the Rabconnectin-3 complex. Mammalian Rabconnectin-3 has two subunits: Rabconnectin-3α and Rabconnectin-3β. Rabconnectin-3α isoforms are homologous to Rav1, but there is no known Rav2 homolog, and the molecular basis of the interaction between the Rabconnectin-3α and β subunits is unknown. We identified ROGDI as a Rav2 homolog and novel Rabconnectin-3 subunit. ROGDI mutations cause Kohlschutter–Tonz syndrome, an epileptic encephalopathy with amelogenesis imperfecta that has parallels to V-ATPase–related disease. ROGDI shares extensive structural homology with yeast Rav2 and can functionally replace Rav2 in yeast. ROGDI binds to the N-terminal domains of both Rabconnectin-3 α and β, similar to Rav2 binding to Rav1. Molecular modeling suggests that ROGDI may bridge the two Rabconnectin-3 subunits. ROGDI coimmunoprecipitates with Rabconnectin-3 subunits from detergent-solubilized lysates and is present with them in immunopurified lysosomes of mammalian cells. In immunofluorescence microscopy, ROGDI partially localizes with Rabconnectin-3α in acidic perinuclear lysosomes. The discovery of ROGDI as a novel Rabconnectin-3 interactor sheds new light on both Kohlschutter–Tonz syndrome and the mechanisms behind mammalian V-ATPase regulation.

V-ATPases are rotary motors that couple the hydrolysis of ATP to the movement of protons across biological membranes. V-ATPases are composed of two subcomplexes, V_1 and V_0. V_0 resides in a membrane and is responsible for the translation of the rotational force from V_1 into proton translocation across the membrane. V_1, which is oriented toward the cytosol and peripheral to the V_0 subcomplex, hydrolyzes ATP, creating rotation of a central stalk that is transmitted to V_0. V-ATPase activity is essential in higher eukaryotes and conditionally lethal in yeast (1, 2). V-ATPases are highly conserved among eukaryotes, including mammals. This broad conservation allows *Saccharomyces cerevisiae* to be used as a model system for studying the V-ATPase. V-ATPase activity has been shown to be important for viral entry into cells, vesicular loading and trafficking, lysosomal/vacuolar degradation, and the progression of some cancers (3). Given the important roles that V-ATPases play, proper regulation of V-ATPase activity is essential. Several different regulatory mechanisms have been identified, including membrane phosphoinositide lipid content, subunit isoform composition, and reversible disassembly (4–6).

In cells, V-ATPases are present as both fully assembled active complexes and disassembled inactive V_1 and V_0 subcomplexes. Conversion between these states can depend on multiple signals and is termed reversible disassembly. In *S. cerevisiae*, glucose deprivation triggers V-ATPase disassembly, whereas the presence of glucose triggers rapid reassembly (6, 7). When the proper conditions are met, V_1 reassembles with V_0 and catalytic activity resumes. The assembly state of mammalian V-ATPases has been found to respond to glucose, amino acids, and luminal pH (8–11).

In yeast, the RAVE complex (composed of Rav1, Rav2, and Skp1) catalyzes V-ATPase assembly (12, 13). Rav1 is the backbone of the RAVE complex and binds to Rav2, Skp1, V_1 subunits (V_1E and G, V_1C), and Vph1 (V_0a) (14). Comparatively less is known about Rav2; it binds to the N-terminal (NT) end of Rav1 (2–240) and has been shown to also bind to Vma5 (14, 15). The current model of RAVE-catalyzed reassembly suggests that RAVE binds to cytosolic V_1, creating a RAVE–V_1 complex. The RAVE–V_1 complex then binds to cytosolic V_1C and ultimately reunites V_1 and V_1C with V_0 on the vacuolar membrane (16). Upon reassembly on the vacuolar membrane, the catalytic activity of both domains resume.

The process of reversible disassembly, like V-ATPase structure, is well conserved among eukaryotes (17, 18). The RAVE complex homolog in higher eukaryotes is Rabconnectin-3. RAVE and Rabconnectin-3 are both required for efficient V-ATPase reassembly but respond to different

* For correspondence: Patricia M. Kane, kanepm@upstate.edu.

signals for assembly and disassembly (19–22). Rabconnectin-3 is a heterodimer composed of two subunits: Rabconnectin-3α and Rabconnectin-3β (23, 24). Each Rabconnectin-3 subunit has two isoforms in mammals. Rabconnectin-3α includes DMXL1 and DMXL2, and Rabconnectin-3β includes WDR7 and possibly WDR72. Based on published expression data, the isoforms for each subunit appear to be expressed differently based on tissue type (25). Both Rabconnectin-3α and Rabconnectin-3β share some structural similarity to Rav1 (26) although Rabconnectin-3α shares additional sequence homology.

We show here that the relatively poorly characterized protein ROGDI is the higher eukaryotic homolog of yeast Rav2. ROGDI mutations cause Kohlschutter–Tonz syndrome (KTS), a homozygous recessive condition characterized by amelogenesis imperfecta, epilepsy, and psychomotor regression (27). We found that ROGDI interacts with the NT region of Rabconnectin-3 subunits and coimmunoprecipitates with DMXL1, WDR7, and the V_1A subunit. ROGDI strongly colocalizes with V_1A and partially colocalizes DMXL1 and lysosomes. We speculate that KTS is a disease resulting from impaired V-ATPase activity; ROGDI mutations impair the activity of the Rabconnectin-3 complex, which in turn results in decreased V-ATPase assembly and activity.

Results

Mammalian ROGDI shares structural and functional homology with yeast Rav2

Although Rav2 is essential for RAVE function in yeast (12), Rabconnectin-3 has long been characterized as a heterodimer with no subunit equivalent to yeast Rav2. Mutations in the ROGDI protein are associated with KTS, but its molecular function was unknown (28). However, the Phyre2 homology server (29) modeled most of the Rav2 sequence onto a crystal structure of ROGDI (30) with high confidence. In addition, ROGDI has been identified in coprecipitates with the V-ATPase and Rabconnectin-3 subunits by mass spectrometry (31, 32). A recent ROGDI knockout mouse both recapitulates the symptoms of KTS and exhibits evidence of altered pH homeostasis (33).

ROGDI and Rav2 are of similar sizes; ROGDI is 287 amino acids (32 kDa) and Rav2 is 351 amino acids (40 kDa). The two sequences are only 20.5% similar (11% direct identity) based on comparison by EMBOSS (34), but a superposition of the AlphaFold (35) models for Rav2 and ROGDI shown in Figure 1*A* highlights striking structural similarities between the proteins. A recent structure of yeast RAVE (15) further supports the strong structural similarity between Rav2 and ROGDI. Both proteins contain two main domains: an α-domain that folds into an atypical leucine zipper and a β-domain that folds into a β-sandwich. Surface loops within these regions contain the most structural diversity. The additional size of Rav2 derives from a domain peripheral to the β-domain (residues 225–300). The functional consequence of these differences is not yet known. However, the substantial structural similarity between the two proteins strongly suggests a common function.

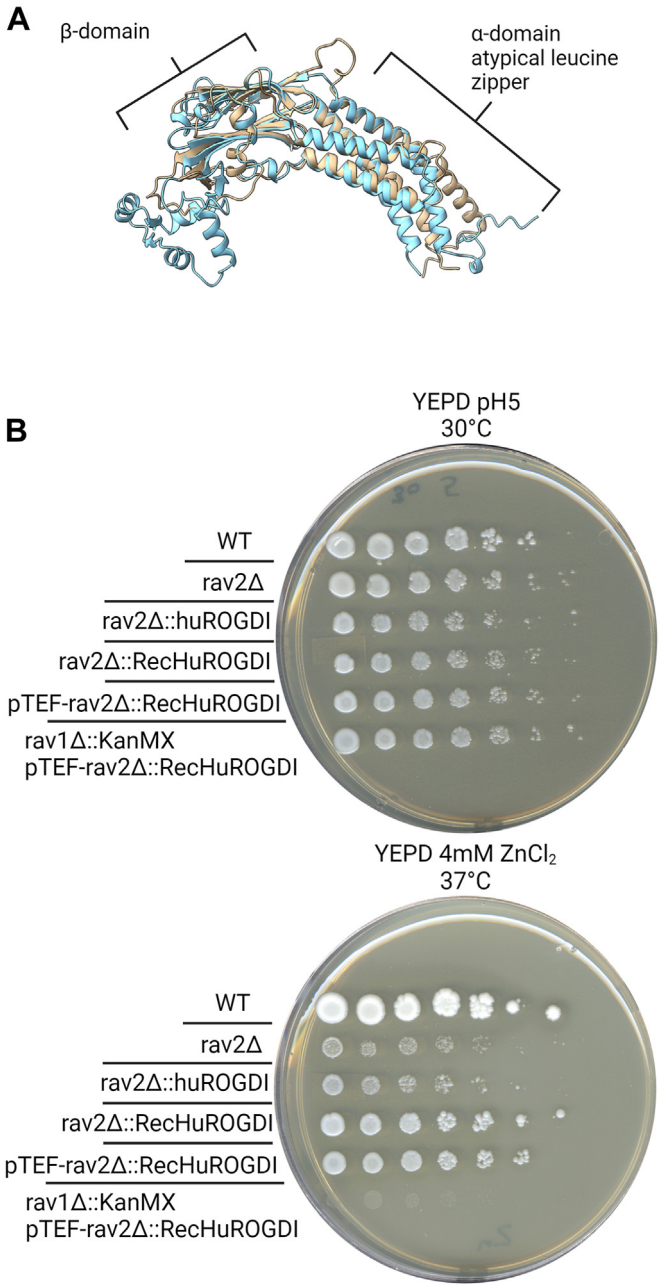

Figure 1. Human ROGDI and yeast Rav2 display structural and functional homology. *A*, superposition of AlphaFold3 models of human ROGDI (*tan*, UniProt ID: Q03956) and yeast Rav2 (*blue*, UniProt ID: Q9GZN7). Models were superimposed with UCSF ChimeraX. Models were retrieved from the AlphaFold Protein Structure Database, identifiable by UniProt ID. *B*, phenotyping of *rav2Δ* and *rav2Δ::ROGDI* containing strains. *rav2Δ*::huROGDI encodes for human ROGDI in place of the *RAV2* open reading frame under control of the native *RAV2* promoter; *rav2Δ*::RecHuROGDI contains human ROGDI recoded for yeast expression in place of the *RAV2* open reading frame; pTEF-*rav2Δ*::RecHuROGDI replaces the native *RAV2* promoter for the strong *TEF* promoter; the *rav1Δ::KanMX* p*TEF-rav2Δ::RecHuROGDI* strain carries a deletion in the RAVE subunit Rav1. YEPD pH 5 at 30 °C (*top*) is permissive for growth of *rav* mutants, YEPD + 4 mM $ZnCl_2$ at 37 °C (*bottom*) inhibits growth of *rav* mutants. YEPD, yeast extract–peptone–dextrose.

Yeast *rav1Δ* and *rav2Δ* deletion mutants exhibit a characteristically weaker version of the Vma⁻ phenotype arising

from loss of V-ATPase activity (13). The *vma* mutants can grow at pH 5 but grow poorly at elevated pH or in the presence of multiple ions including Zn^{2+}. *vph1Δ* mutants, which lack a vacuole-specific V-ATPase subunit isoform, show some growth at elevated pH but fail to grow in plates containing 4 mM $ZnCl_2$. RAVE is an isoform-specific assembly factor, only catalyzing assembly of Vph1 containing V-ATPases, and *rav* mutants also fail to grow in elevated zinc concentrations (36).

Replacement of the *RAV2* open reading frame with the human ROGDI complementary DNA (cDNA) partially rescues the Rav$^-$ phenotype of a *rav2Δ* mutant as shown in Figure 1*B*. We also expressed a yeast codon–optimized ROGDI from the *RAV2* promoter (RecHu ROGDI). This further rescued the Rav$^-$ phenotype compared with human ROGDI cDNA. Replacement of the native *RAV2* promoter, which is relatively weak, with the strong *TEF* promoter slightly improved growth. To confirm that ROGDI was acting as part of the yeast RAVE complex rather than as a bypass suppressor, we deleted *RAV1* in the TEF-RecHu ROGDI strain. In this strain, any rescue by ROGDI is abolished, indicating that ROGDI may function as part of the RAVE complex in a Rav2-like manner.

ROGDI interacts with structurally conserved NT β-propeller in yeast two-hybrid assay

We hypothesized that ROGDI might bind to Rav1, based on the complementation of the *rav2Δ* phenotype, and possibly to one or more of the Rabconnectin-3 subunits. There are no experimental structures of Rabconnectin-3 subunits available. Secondary structure comparisons of the Rabconnectin-3 subunits to Rav1 are shown in Figure 2*A*. The NT region of Rav1 forms two β-propellers (37), and both Rabconnectin-3 subunits are predicted to be rich in β-sheets and to contain WD-40 repeats that form β-propellers. In addition, in all three proteins, following the β-propellers is an α-solenoid domain. The α-solenoid of Rav1 is responsible for binding to the V_1E and V_1G subunits (14). This region has the highest homology between Rav1 and Rabconnectin-3α. There are additional regions of homology within the β-propeller region and a 6 amino acid sequence necessary for Rav1 to bind to Vph1 (26). Specifically, it appears that Rav1 residues 2–240 are indispensable for Rav2 binding (14) and are conserved in Rabconnectin-3α. In the cryo-EM structure of RAVE–V_1, residues 2–240 localize to the first β-propeller and Rav2 binds in this region (37). Considering the overall structural conservation of ROGDI to Rav2 and Rav1 to Rabconnectin-3, we hypothesize that ROGDI interacts with the similar regions of Rabconnectin-3.

We generated yeast two-hybrid constructs containing the NT β-propeller regions of DMXL2, WDR7, WDR72, and Rav1. With this yeast two-hybrid system (38), fusion proteins with the Gal4-activating and -binding domains drive expression of genes under control of the *GAL1* and *GAL2* promoters when they interact. Growth on medium lacking adenine and histidine (supplemented minimal medium [SD]-Trp, Leu, Ade, His) can then be used as a readout for protein–protein interactions. Figure 2*B* shows growth for strains containing

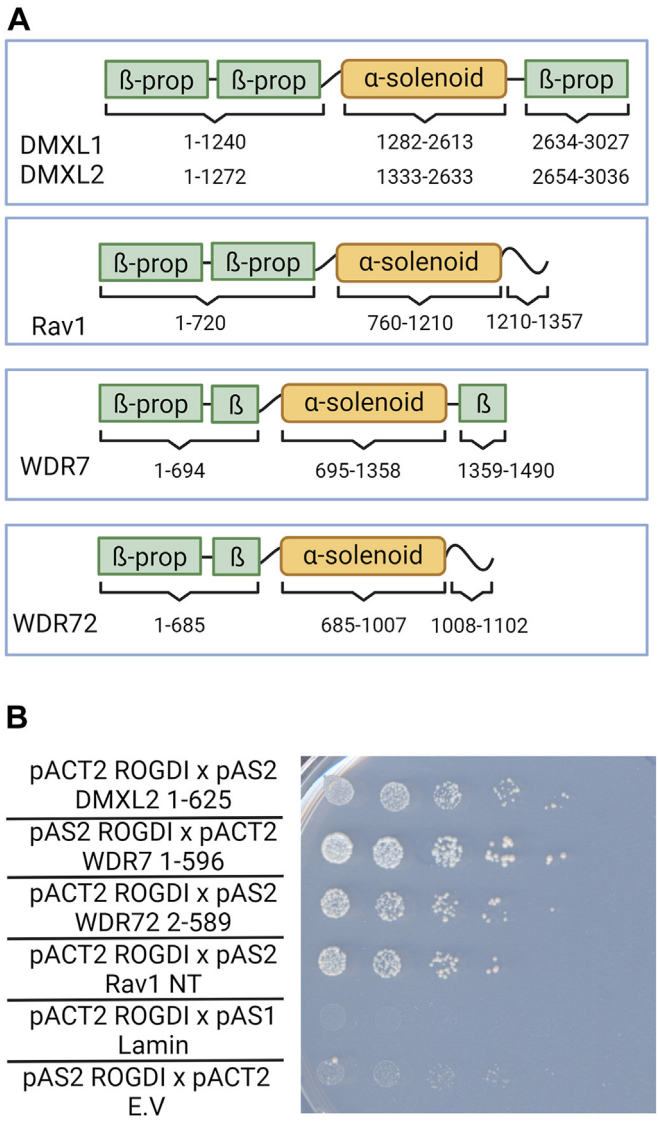

Figure 2. ROGDI interacts with conserved β-propeller region of Rav1 and Rabconnecin-3. *A*, secondary structure comparison of Rabconnectin-3α, Rabconnectin-3β, and Rav1. Regions that are modeled to form β-propellers and α-solenoid are indicated with corresponding amino acid positions. *B*, fusion proteins of ROGDI, DMXL2 1–625, WDR7 1–596, WDR72 1–589, and Rav1 2–720 were generated in pAS2 and pACT2 plasmids as described in the Experimental procedures section. All pACT2 plasmids were transformed into the PJ69-4α two-hybrid strain, and pAS2 plasmids were transformed into PJ69-4a yeast two-hybrid strain. Diploids were selected on SD media lacking leucine and tryptophan (SD- Trp, Leu). Growth on test media lacking tryptophan, leucine, histidine, and adenine (SD- Trp, Leu, Ade, His) is shown and indicates protein–protein interactions between the fusion proteins. pACT2 vector only and pAS1-lamin were used as negative controls.

ROGDI and DMXL2 NT, WDR7 NT, WDR72 NT, and Rav1 NT, but there is no growth when ROGDI is combined with control vectors pACT2 and pAS1-lamin. These data indicate that ROGDI binds to the indicated NT regions of DMXL2, WDR7, WDR72, and Rav1. ROGDI binding to Rav1 is consistent with the ability for ROGDI to partially rescue growth under Rav- conditions in a *rav2Δ* mutant shown in Figure 1*B*. Furthermore, these results suggest that ROGDI binds to both DMXL2, which has direct sequence homology with Rav1, and WDR7 and WDR72, which do not.

ROGDI interactions with Rabconnectin-3 and V-ATPase subunits

ROGDI is modeled to interact with both Rabconnectin-3 subunits

The molecular nature of the interaction between the Rabconnectin-3 subunits is not understood. A stable complex between Rabconnectin-3α and Rabconnectin-3β was identified by Kawabe *et al.* in 2003 (23). However, it is not known whether there are additional members of the complex. Since one of the major differences between human Rabconnectin-3 and yeast RAVE is the apparent duplication of the Rav1-like subunit, we are not able to look to yeast as a model system. ROGDI displays yeast two-hybrid interactions between the NT domain of both Rabconnectin-3α and β subunits (Fig. 2*B*). We speculate that ROGDI may serve a bridging function, connecting the two Rabconnectin-3 subunits. To begin investigating the interaction between ROGDI, DMXL1 NT, and WDR7 NT, we used AlphaFold Multimer (39) to model the three proteins together. WDR7 and DMXL1 were chosen as they are the more ubiquitously expressed isoforms (25). The top result is a model that includes ROGDI interacting with β-propellers from both DMXL1 NT and WDR7 NT (Fig. 3). WDR7 is modeled to include 1.5 NT propellers in the NT region, whereas DMXL1 is modeled to include two full propellers, like Rav1. ROGDI is positioned between the face of the full propeller of WDR7 with the half propeller contracting the ROGDI α-domain. DMXL1 is modeled to contact the ROGDI α-domain opposing WDR7, with ROGDI making contacts with first DMXL1 ß-propeller. The DMXL1–ROGDI interaction is similar to the interaction between Rav1 and Rav2 (37). There are few contacts modeled between DMXL1 and WDR7; consistent with this, we have not observed interactions between Rabconnectin-3α and β subunit isoforms in yeast two-hybrid experiments. Further investigation is needed to experimentally confirm the details of this modeled interaction, but we sought support for a trimeric complex by immunoprecipitating DMXL1 from a mammalian cell system and probing for its partner proteins.

DMXL1 coimmunoprecipitates WDR7, ROGDI, and V_1 subunit A

Both ROGDI and the Rabconnectin-3 subunits are highly conserved among mammals. We immunoprecipitated DMXL1 from a mouse breast cancer cell line previously used to study the V-ATPase (40). DMXL1 is a large protein (predicted molecular mass of 337 kDa). Only a ∼200 kDa fragment was detectable in the input in Figure 4, but the full-length protein was detected in postnuclear supernatants in later experiments, and the specificity of this anti-DMXL1 polyclonal antibody was previously validated in experiments with a kidney DMXL1 knockdown strain (41). The anti-DMXL1 antibody immunoprecipitated both the ∼200 kDa fragment and full-length DMXL1. In addition, WDR7, ROGDI, and V_1A coimmunoprecipitated with DMXL1 (Fig. 4). None of these proteins was immunoprecipitated with a nonspecific isotype control. These data suggest that ROGDI is present in complexes with DMXL1, WDR7, and the V-ATPase.

Cellular localization of ROGDI and DMXL1

In *S. cerevisiae*, RAVE binds to V_1 in the cytosol and Rav1 and Rav2 are reversibly recruited to vacuolar membrane as a complex under assembly conditions (14, 42). We investigated the intracellular localization of ROGDI and the V-ATPase V_1A subunit using direct immunofluorescence microscopy (Fig. 5*A*). Both ROGDI and V_1A exhibit diffuse cytosolic staining and puncta, with an enrichment in puncta adjacent to the nucleus. Merging the ROGDI and V_1A channels shows substantial overlap between ROGDI and V_1A in the perinuclear region and further toward the cell periphery. Colocalization of the two proteins is supported by line scan profiles from the ROGDI and V_1A channels in which there is an increase in pixel intensity at similar locations along lines drawn adjacent to the cell nucleus and more peripherally. There data suggest that, ROGDI, like Rav2, partially colocalizes with V_1 subunits on intracellular compartments. As shown in Figure 5*B*, the lysosomal membrane marker lysosome-associated membrane protein 2 (LAMP2) labels puncta throughout the cell (peripheral lysosomes) and is concentrated adjacent to the nucleus (perinuclear lysosomes). A similar distribution of peripheral and perinuclear lysosomes has been seen in other cell types (43, 44). Staining the same cells with the fixable LysoTracker Red DND-99 pH indicator, which accumulates in acidified lysosomes (45), reveals prominent labeling of the perinuclear LAMP2-containing lysosomes, indicating that they are strongly acidic. However, there is also labeling of peripheral lysosomes.

Confocal immunofluorescence images in Figure 6*A* demonstrate that ROGDI extensively colocalizes with LAMP2, particularly in the perinuclear region, with a Pearson's *R* value of 0.78 for the boxed area. ROGDI–LAMP2 puncta are present

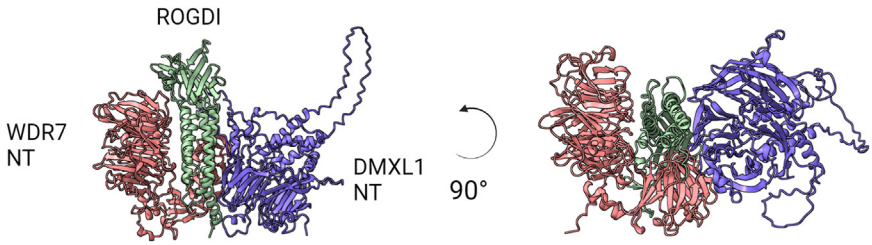

Figure 3. AlphaFold3 model of ROGDI binding to N-terminal (NT) domains of Rabconnectin-3α and β. AlphaFold3 model of DMXL1 NT (amino acids 1–630), WDR7 NT (1–600), and full-length ROGDI. The ipTM for this model is 0.82 and pTM is 0.81, as described in the Experimental procedures section. These reflect a high confidence model. ipTM, interface predicted template modeling; pTM, predicted template modeling.

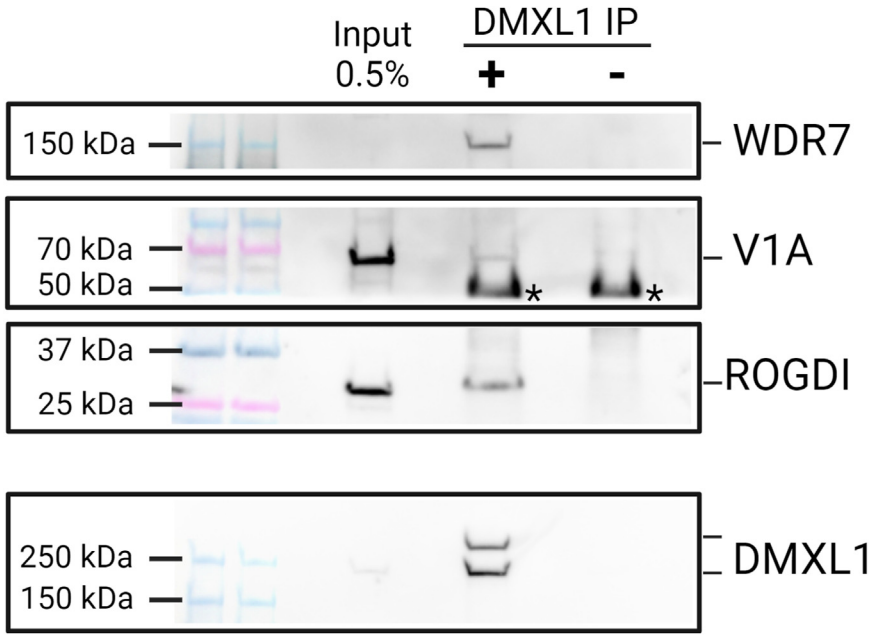

Figure 4. DMXL1 coimmunoprecipitates ROGDI, WDR7, and V_1 subunit A. DMXL1 immunoprecipitation from mouse 4T1 cells was performed as described in the Experimental procedures section. Anti-DMXL1 antibody (+) or an equal amount of nonspecific rabbit IgG (–) were separately bound to equal volumes of protein-A Dynabeads. 4T1 cells were lysed and subjected to crosslinking as described in the Experimental procedures section. The total lysate (0.5%) was run on the gel as indicated. The IgG–Dynabead complexes were incubated with equal volumes of 4T1 lysate at 4 °C with agitation. Samples were eluted from beads by heating at 98 °C in the presence of cracking buffer and then analyzed by SDS-PAGE and Western blotting with the indicated antibodies. The top three images were cut from the same blot, then probed with antibodies. The * on the V_1A blot indicates the antibody heavy chain. The *bottom image* is from a separate blot. Molecular mass standards are shown at the *left*.

peripherally but are less numerous. ROGDI also displays some diffuse cytosolic staining in Figure 6*A*, suggesting that not all ROGDIs are associated with membranes, consistent with wide-field fluorescence images in Figure 5*A*. We also assessed the colocalization of DMXL1 and ROGDI directly (Fig. 6*B*) and see strong colocalization in the perinuclear region. The Pearson's *R* value of 0.64 between ROGDI and DMXL1 is consistent with colocalization in this region although it is slightly lower than the *R* value for ROGDI and LAMP2 (Fig. 6*A*). Overall, DMXL1 localizes to puncta in the cytosol, along with some nuclear signal, which is unlikely to be associated with endolysosomal or V-ATPase function and may be artifactual. DMXL1 and LAMP2 immunofluorescence images are directly compared in Fig. S1*A* and show a level of overlap similar to ROGDI and DMXL1. Taken together, the data suggest that both ROGDI and DMXL1 localize strongly to perinuclear lysosomes, but ROGDI also appears to have a diffuse cytosolic population that may not be bound to any membrane.

To investigate the subcellular distribution of ROGDI, WDR7, DMXL1, and V_1 subunit A further, we first used subcellular fractionation. Cells were lysed in the absence of detergent, and the supernatant from a low-speed centrifugation was separated into membrane and soluble fractions by high-speed centrifugation. Figure 7*A* demonstrates that Rabconnectin-3 subunits, WDR7 and DMXL1, are almost entirely in the membrane fraction with relatively little free in the cytosol (Fig. 7*A*). In contrast, ROGDI is largely in the supernatant, whereas a minor population is membrane associated.

We also isolated a lysosomal fraction by LysoIP (lysosomal immunoprecipitation), using the hemagglutinin (HA)-tagged lysosomal protein TMEM192 to affinity purify lysosomes from a cell lysate (46) (Fig. S1*B* shows that TMEM192 localizes to the lysosomal membrane in these cells.). Figure 7*B* compares the distribution of Rabconnectin-3 subunits, V-ATPase subunits, the lysosomal protein LAMP1, and endosomal protein EEA1, as well as the FLAG-TMEM192 used for immunoprecipitation, in the input sample, two washes, and the final LysoIP sample. The ratio of the LysoIP to lysate signal is shown for each protein. The ratios for FLAG-TMEM192 and the lysosomal marker LAMP1 are similar. The V_0 membrane subunit d1 is strongly enriched in the LysoIP. Two V_1 subunits (V_1A and V_1E1) are present but less enriched, consistent with their peripheral membrane localization; these subunits are likely to be part of assembled V-ATPase complexes. DMXL1 coisolates to a similar extent as LAMP1 in the LysoIP sample, suggesting it is coprecipitated with the lysosomal membranes. ROGDI is also present in the LysoIP samples but at somewhat lower proportion of the total than the V_1 subunits. Although WDR7 is present in both the membrane fraction in Figure 7*A* and the LysoIP, the antibody is weak, making quantitative assessment difficult. The apparent very strong enrichment of endosomal protein EEA1 was unexpected, but given the nature of endolysosomal compartments, it is possible either that TMEM192 is also present in endosomes or that EEA1 can escape to lysosomes. Overall, these results are consistent with localizations observed in Figures 5 and 6 and suggest that although ROGDI can associate with Rabconnectin-3 subunits, DMXL1 and WDR7, it may not always associate with them in

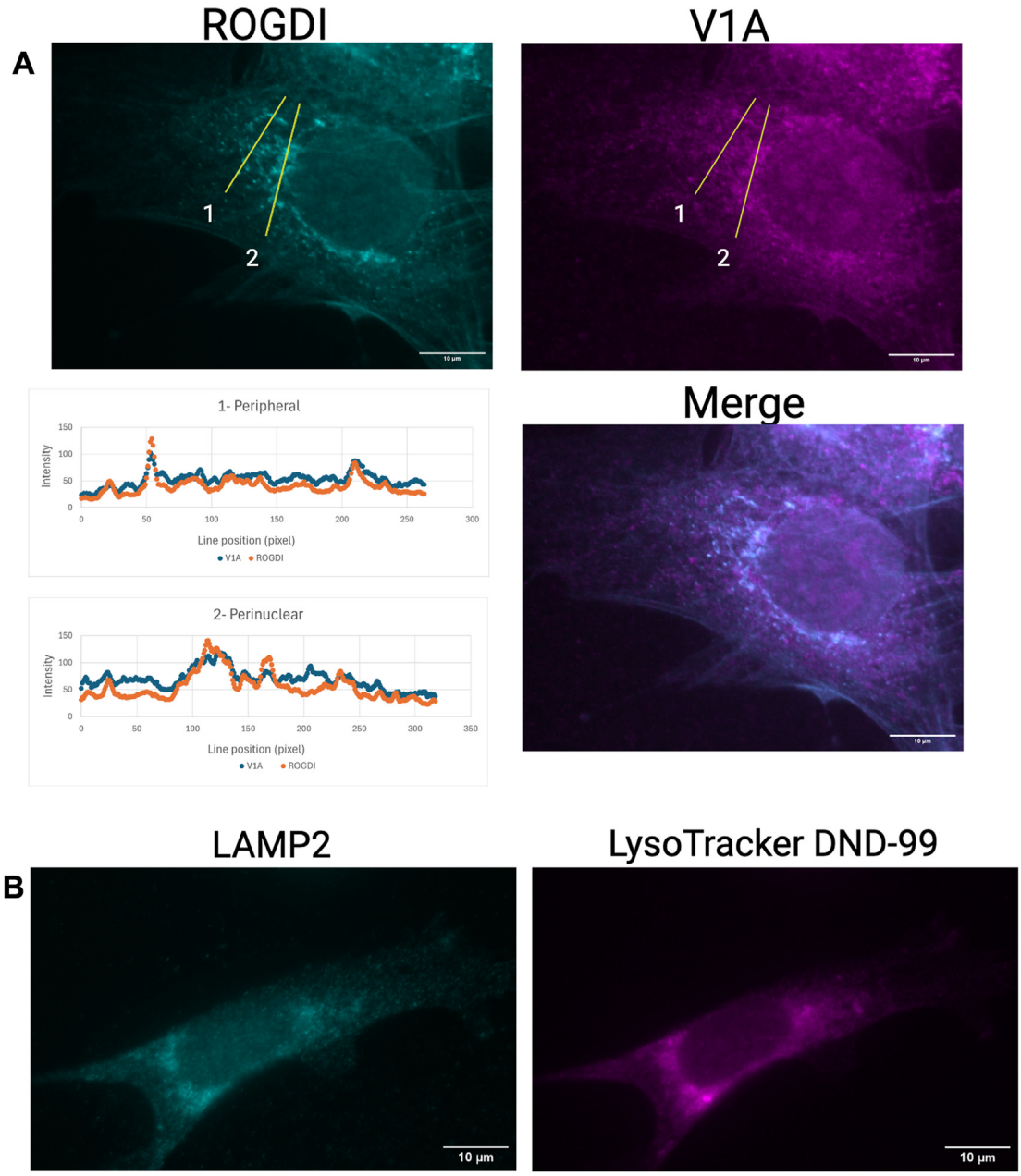

Figure 5. ROGDI partially localizes with V_1A on perinuclear lysosomes. *A*, wide-field immunofluorescence micrographs of 4T1 cells costained with directly labeled anti-V_1 A subunit (*magenta*) and anti-ROGDI (*cyan*) antibodies as described in the Experimental procedures section. Two lines were drawn through ROGDI puncta both in the peripheral (1) and perinuclear (2) regions. Fluorescence intensity along each line is plotted; ROGDI is *orange* and V_1A is *blue*. Graph 1 corresponds to peripheral puncta, and graph 2 corresponds to perinuclear puncta. A merged image combining the ROGDI and V_1A channels is at the *right* of the line scan plots. *B*, immunofluorescence micrograph of 4T1 cells costained with anti-LAMP2 (*cyan*) antibody and fixable LysoTracker DND-99 (*magenta*), an indicator of lysosomal acidification. Cells were stained with LysoTracker DND-99 immediately prior to fixation and permeabilization. Permeabilization and fixation were performed as in Figure 5*A*. Both images are from a wide-field microscope. LAMP2, lysosome-associated membrane protein 2.

the cell. Like the V-ATPase V_1 subcomplex, ROGDI can be present both in the cytosol and on the lysosomal membrane.

Discussion

The work described here shows that the structural similarity between mammalian ROGDI and yeast Rav2 (37) extends to function, as indicated by the ability of human ROGDI to complement a *rav2Δ* mutant in yeast. In parallel with the interaction of Rav2 with the NT β-propeller of Rav1, ROGDI exhibits two-hybrid interactions with the β-propeller domains of both Rav1 and Rabconnectin-3α subunit DMXL2, which share sequence homology. Previous work indicated that amino acids 1 to 240 of Rav1 were required for Rav2 binding (14) and the recent cryo-EM structure of RAVE places Rav2 on the third and fourth blades of the first propeller in Rav1 (15). The AlphaFold3 model (47) of Rabconnectin-3 (Fig. 3) independently indicates an interaction with ROGDI with a similar region in first NT propeller in DMXL1, suggesting that this

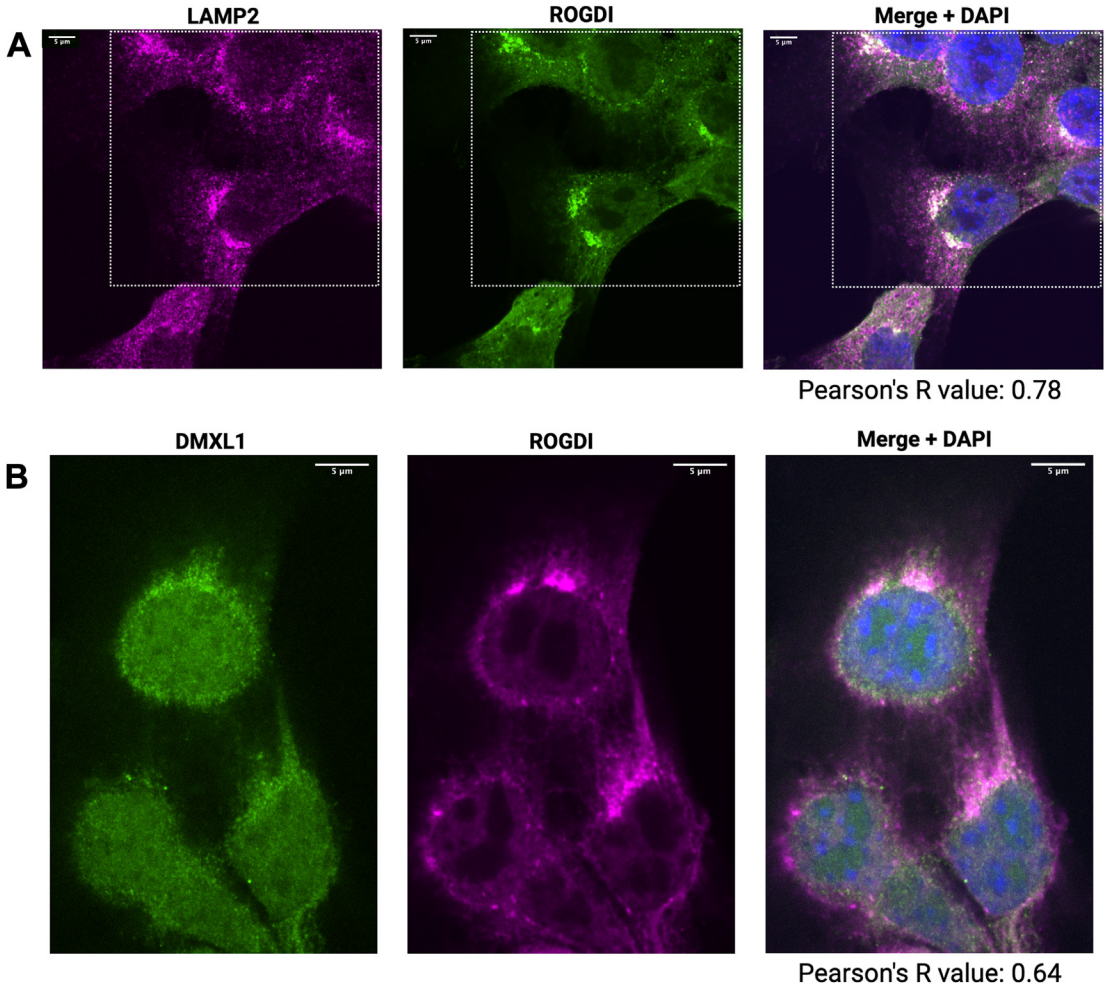

Figure 6. DMXL1 and ROGDI partially colocalize on perinuclear lysosomes. *A*, immunofluorescence micrograph of a 4T1 cell costained with indirectly labeled anti-LAMP2 (*magenta*) and directly labeled anti-ROGDI (green) antibodies. LAMP2 serves as a lysosomal marker. Images are from a single slice of a confocal stack. The composite image with DAPI (*blue*) shown to the *right* illustrates extensive overlap between the anti-LAMP2 and anti-ROGDI channels on perinuclear lysosomes. The *dotted line* indicates the region of interest used for determination of Pearson's value. *B*, immunofluorescence micrograph of a 4T1 cell costained with indirectly labeled anti-LAMP2 (*magenta*) and directly labeled anti-DMXL1 (green) antibodies. The composite image to the *right* shows overlap between the anti-LAMP2 and anti-DMXL1 channels. For both *A* and *B*, the Pearson's *R* value was calculated as described in the Experimental procedures section. DAPI, 4′,6-diamidino-2-phenylindole; LAMP2, lysosome-associated membrane protein 2.

interface is similar between RAVE and Rabconnectin-3. There is no homolog of either Rabconnectin-3β isoform in the yeast genome, and although Rabconnectin-3α and β isoforms are isolated together, the details of their molecular interaction are not known. As noted previously (26), Rabconnectin-3α and β have similar secondary structures, characterized by predicted β-propellers in the NT half and an α-solenoid region in the C-terminal half but no direct sequence homology. The two-hybrid assay in Figure 2 indicates that the first NT β-propeller of WDR7 interacts with ROGDI, and this interaction is also seen in the AlphaFold3 model, along with interactions of a second NT "half-propeller." The model in Figure 3 contains only the NT domains of DMXL1 and WDR7, but Fig. S2 shows a model of the complete DMXL1, WDR7, and ROGDI complex. Importantly, both models suggest that ROGDI bridges the NT regions of Rabconnectin-3α and 3β subunits. Removal of ROGDI from the model in Fig. S2 reveals relatively few direct interactions between the two Rabconnectin-3 subunits. Further validation of this model is required, but as described later, the phenotypes accompanying loss of ROGDI *in vivo* would be compatible with functionally significant interactions with both Rabconnectin-3 subunits.

Through immunofluorescence microscopy and subcellular fractionation of mouse 4T1 cells, we found that DMXL1 appears to be primarily membrane bound and enriched in lysosomes. WDR7 also appears to be membrane bound. ROGDI coimmunoprecipitates with DMXL1, is present in lysosomal membrane fractions, and shows strong colocalization with lysosomal marker LAMP2 in immunofluorescence microscopy, but a substantial proportion of ROGDI is soluble and cytosolic. Significantly, none of these proteins has apparent transmembrane domains. Rabconnectin-3 complexes containing DMXL2 and WDR7 are highly expressed in brain and enriched at the presynaptic region of neurons (48, 49) and in the dense core vesicles of neuroendocrine cells (50). In the latter, both DMXL2 and WDR7 appear to be membrane bound, but WDR7 is implicated in recruitment of DMXL2 to the membrane (50). Subcellular localization of DMXL1 has not

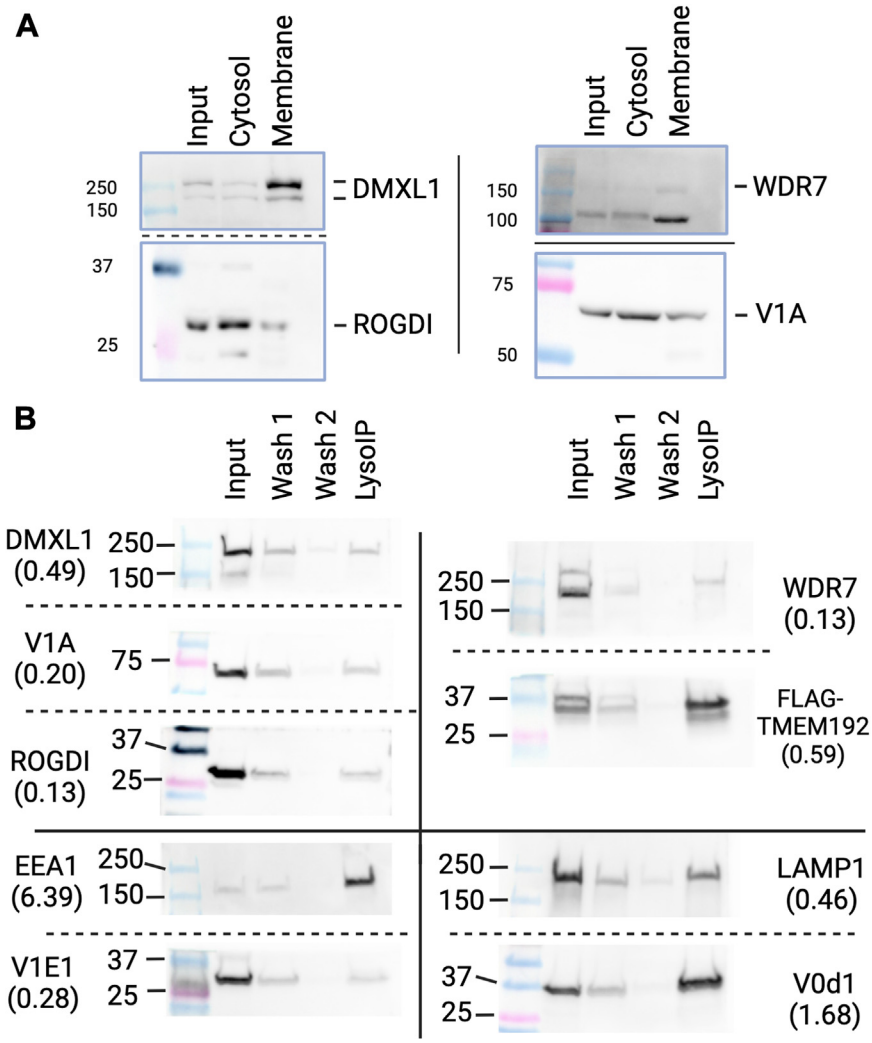

Figure 7. Subcellular distribution of ROGDI and Rabconnectin-3. *A*, subcellular fractionation of 4T1 cell lysate. Cells were lysed mechanically by passing through a 27-gauge needle and centrifuged at 10,000*g* to pellet nuclei and mitochondria. A portion of the resulting postmitochondrial supernatant was reserved as input as described in the Experimental procedures section. The postmitochondrial supernatant was then centrifuged to pellet membranes and supernatant (cytosol). Both the membrane pellet and cytosolic samples were denatured and analyzed by SDS-PAGE and Western blotting with antibodies against the indicated proteins. Molecular mass markers are shown on *left*. All samples were run on a single SDS-PAGE gel, and immunoblots probed anti-ROGDI and anti-DMXL1 blots were cut at the 50 kDa molecular mass marker. *B*, a lysosomal fraction was isolated by affinity purification using FLAG-tagged TMEM192 from mechanically lysed 4T1 cells as described in the Experimental procedures section. Cells were transiently transfected with pCDNA3-TMEM192-FLAG-HA, and a postmitochondrial supernatant was generated as in *A*. A portion of this sample was set aside as input. Lysosomes were isolated by binding to anti-HA nanobody magnetic beads. Input (0.75% of total), sequential washes of the beads (washes 1 and 2), and the final eluted sample (LysoIP) were separated by SDS-PAGE and analyzed by immunoblotting with the indicated antibodies. Samples separated by *dotted lines* were from the same gel, cut at the position of the line. Intensities of the lysate and LysoIP samples for each sample were determined using FIJI, and the ratio of LysoIP/lysate intensity is shown below the protein label. The data shown are representative of three independent experiments. HA, hemagglutinin; LysoIP, lysosomal immunoprecipitation.

been explored previously, but the data presented here are consistent with lysosomal association in 4T1 cells. We cannot compare the cellular levels of DMXL1 and ROGDI from these data, so it is possible that ROGDI is nearly stoichiometric with DMXL1 at the membrane and "excess" ROGDI is soluble and cytosolic. However, it is also possible that ROGDI is not always associated with the other Rabconnectin-3 subunits. This would be a significant difference from the yeast RAVE complex, where Rav2 and Rav1 form a stable complex that associates with cytosolic V_1 and both subunits are required for glucose-dependent recruitment to the vacuolar membrane and V-ATPase assembly (16, 51). A substantial proportion of the V_1 subunit A (likely present as part of V_1 subcomplexes) is cytosolic in the 4T1 cells, as in many mammalian cell lines (8, 52). Further experiments will be needed to determine whether ROGDI reversibly associates with Rabconnectin-3α and β at lysosomal membranes, possibly in combination with V_1, and the effect of these associations on V-ATPase assembly and function.

We made four separate attempts to knock out ROGDI with CRISPR–Cas9 and two different guide RNAs but were unable to generate a ROGDI knockout in the mouse 4T1 breast cancer cells. However, other existing evidence associates ROGDI, as well as Rabconnectin-3α and β, with the V-ATPase function in acidification. DMXL1 and WDR7 coimmunoprecipitated with the V_1B1 subunit from kidney, and

RNAi of DMXL1 affected organelle acidification (31). ROGDI was also coimmunoprecipitated with V_1B1 at lower levels. Similarly, ROGDI, along with DMXL2 and WDR7, was isolated with the V-ATPase from a synaptic vesicle fraction (32), where assembly of V-ATPases drives vesicle acidification and neurotransmitter loading (11). The localization of ROGDI and DMXL1 to perinuclear lysosomes in 4T1 cells shown here is consistent with enrichment of ROGDI and Rabconnectin-3 in areas of V-ATPase assembly. Perinuclear lysosomes are highly acidic in the 4T1 cells, as indicated by LysoTracker staining (Fig. 5*B*). This population of lysosomes has been demonstrated to be a site of V-ATPase reassembly in other cells (44, 53). We propose that complexes containing ROGDI, DMXL1, and WDR7 promote association of V_1 subcomplexes with V_o subcomplexes at sites of ongoing acidification, including perinuclear lysosomes as well as synaptic vesicles.

Human disease phenotypes and mouse models also indicate that ROGDI could affect V-ATPase–driven acidification in combination with Rabconnectin-3α and β isoforms. Complete loss-of-function mutations in human ROGDI cause KTS, characterized by severe epilepsy, developmental delay, amelogenesis imperfecta (defects in tooth enamel formation), and in some cases, kidney disease (28, 54). Many of these phenotypes are recapitulated in a recent ROGDI knockout mouse model, which exhibited susceptibility to seizures, defective enamel formation, digestive problems, and in most cases, death before 12 weeks of age (33). Importantly, these authors associate these phenotypes with defects in pH homeostasis likely to involve V-ATPase activity. DMXL2 knockout mice develop normally but die shortly after birth of neurological defects that prevent feeding (55). A DMXL1 knockout appears to be lethal in mice (56). Taken together, these data suggest that complete loss of ROGDI may be somewhat better tolerated than complete loss of either of the Rabconnectin-3α isoforms. A mouse kidney–specific DMXL1 knockdown exhibited an incomplete distal renal tubule acidosis (DRTA) (56). Mutations in several kidney-enriched V-ATPase subunit isoforms also result in DRTA (57), whereas mutations in Rabconnectin-3β isoform WDR72 are associated with both DRTA and amelogenesis imperfecta (58–60). It is intriguing that patients with KTS exhibit neurological symptoms associated with defects in Rabconnectin-3α (DMXL2) and kidney and tooth phenotypes characteristic of Rabconnectin-3β (WDR72). This combination of phenotypes could be consistent with ROGDI structurally bridging Rabconnectin-3α and β. Loss of ROGDI may destabilize the Rabconnectin-3 complex and compromise its V-ATPase assembly function. The compromised Rabconnectin-3 complex may still catalyze V-ATPase reassembly but less efficiently than the fully functional complex. This could explain why complete loss of Rabconnectin-3α is more severe than the loss of ROGDI in mice.

Experimental procedures

Materials and media

Oligonucleotides were purchased from Eurofins Genomics. Anti-ROGDI (catalog no.: ab184954, rabbit) antibody and anti-ATP6V_1A antibody (catalog no.: ab199326, rabbit) were purchased from Abcam. DMXL1 polyclonal antibody (catalog no.: 24413-1-AP, rabbit) for use in immunoblotting, WDR7 polyclonal antibody (catalog no.: 24413-1-AP, rabbit), ATP6V0d1 polyclonal antibody (catalog no.: 18274-1-AP, rabbit), ATP6 V1E1 (catalog no.: 5280-1-AP, rabbit), LAMP1 (catalog no.: 21997-1-AP, mouse), EEA1 (catalog no.: 68065-1-Ig, mouse), and horseradish peroxidase (HRP)–conjugated DYKDDDDK (FLAG tag) monoclonal antibody (catalog no.: HRP-66008, mouse) were purchased from Proteintech. Anti-DMXL1 polyclonal antibody (catalog no.: NBP1-90998, rabbit) was purchased from Novus Biologicals and used in immunofluorescence microscopy. Anti-LAMP2 (ABL-93) was purchased from the Developmental Studies Hybridoma Bank. Anti-HA nanobody M-270 magnetic beads were purchased from Proteintech (atd). Q5 Hot Start polymerase was purchased from New England Biolabs (catalog no.: M0493S). Phire Plant Direct PCR master mix was purchased from ThermoFisher Scientific (F130WH). Human ROGDI cDNA (clone ID: 3861570), DMXL2 (clone ID: 9053066), and WDR72 (clone ID: 8069120) were purchased from Horizon Discovery. WDR7 cDNA was purchased from Genscript (clone ID: OHu06923). Yeast codon-optimized ROGDI was synthesized by Genscript. Yeast and cell culture media were purchased from Fisher Scientific. Other reagents were purchased from MilliporeSigma.

Yeast strains

Yeast strains that were used in this work are listed in Table 1. All yeast strains (other than those used for two-hybrid assay) were constructed in the SF838-5A wildtype background. Yeast genomic integrations were done using PCR constructs with at least 50 bp of flanking homologous sequence to target the construct into the genome. Oligonucleotides used in this study are listed in Table 2. Q5 Hot Start polymerase from New England Biolabs was used to amplify constructs for yeast transformation. Yeast cells were transformed using a lithium acetate protocol (61). Genotyping was done using Phire Plant Direct PCR Master Mix (as described in by the manufacturer).

Table 1
Yeast strains and genotypes

Strain	Genotype
SF838-5Aα	*MATα leu2-3, 112; ura3-52; ade6*
rav2Δ	SF838-5Aα *rav2Δ::URA3*
rav2Δ::huRogdi	SF838-5Aα *rav2Δ*::huRogdi
rav2Δ::RecHu Rogdi	SF838-5Aα *rav2Δ*::RecHu Rogdi
TEF-*rav2Δ*::RecHu Rogdi	SF838-5Aα *natNT2-TEF-rav2Δ*::RecHu Rogdi
rav1Δ TEF-*rav2Δ*::RecHu Rogdi	SF838-5Aα *rav1Δ::kanMX4 natNT2-TEF-rav2Δ*::RecHu Rogdi
PJ69-4a	*MATa trp1-901 leu2-3112 ura3-52 his3-200 gal4 gal80 LYS2::GAL1-HIS3 GAL2-ADE2 met2::GAL7-lacZ*
PJ69-4α	*MATα trp1-901 leu2-3112 ura3-52 his3-200 gal4 gal80 LYS2::GAL1-HIS3 GAL2-ADE2 met2::GAL7-lacZ*

Table 2
Oligonucleotides used

Name	Sequence (5′-3′)
RAV2URA3F	GTG AAT TAC AAA ATT ATA GTA TCT GAT CAA GCA CAC AGT GGA AGT GCT CGA AAA GCA ATC TGA GAG TGC ACC ACG CTT TTC
RAV2URA3R	CTC TTT ATC CAG TTT GTA TTA TAA ATT ATT GTT AAT GTT ATC GCT AGT AGA TTA TTA GTT TTG CTG GCC GCA TCT TCT
URA-int	CCTTAGCATCCCTTCCCTTTG
RAV2-RogdiFnew	GTG AAT TAC AAA ATT ATA GTA TCT GAT CAA GCA CAC AGT GGA AGT GCT CGA AAA GCA ATA TGG CCA CCG TGA TGG CAG CGA C
Rav2-Rogdi Rev	CTC TTT ATC CAG TTT GTA TTA TAA ATT ATT GTT AAT GTT ATC GCT AGT AGA TCA GAA GGG TCT GTA GCT CCA
HuRogdi IntR	GCA TGC AGC TGG TAC ACC GT
Rav2RogdirecodeF	GTG AAT TAC AAA ATT ATA GTA TCT GAT CAA GCA CAC AGT GGA AGT GCT CGA AAA GCA ATA TGG CCA CCG TTA TGG CTG CT
Rav2RogdirecodeR	CTC TTT ATC CAG TTT GTA TTA TAA ATT ATT GTT AAT GTT ATC GCT AGT AGA TCA GAA TGG TCT GTA AGA CCA
Rogdirecode intR	ACC ACC TGC TGG TCT AAA GTT CTT
YDR1-1 (rav2)	GTTGTACCGAGGTTCCATTG
rav2-c4	GGGTCAAGAATACGAAGGCAG
Rogdirecode intR	ACC ACC TGC TGG TCT AAA GTT CTT
YJR1-7	CCATCTCCTCCCTCGGATCAAACTTTC
YJR6-12	CGTTCCTAACAGAGATCAAGC
NatR forward	ACATGGAGGCCCAGAATACCC
NatR reverse	CAGTATAGCGACCAGCATTCAC
RogdipAS2F	GGT CAT ATG GAG GCC CCG GGA ATG GCC ACC GTG ATG GCA GCG AC
RogdipAS2R	GCT TGG CTG CAG GTC GAC GGA TCC GAT CAG AAG GGT CTG TAG CTC CA
RogdipACT2R	GAT CTC TCG AGC TCG AAT TCG GAT GAT CAG AAG GGT CTG TAG CTC CA
WDR721-589pACT2rev	GCT TGG CTG CAG GTC GAC GGA TCC GCC TGT TTC AAT TTC CCA GAT
WDR721-589pACT2R	GAT CTC TCG AGC TCG AAT TCG GAT GCC TGT TTC AAT TTC CCA
WDR7 1F	CATATGGCCATGGAGGCCCCGGGAATGGCAGGAAACAGCCTTGTTCTACC
WDR7 pAS2 596R	GCTTGGCTGCAGGTCGACGGATCCACGATCCAATGCACCAGTATCCAT
Rbcn3a 1-625F	CATATGGCCATGGAGGC CCCGGGAACAGAGGGAAACGGCTCTCGCAGC
Rbcn3a 1-625R	GCTTGGCTGCAGGTCGACGGATCCTGTGGCTGTGATCCGTGAGGACTG
MuTMEMF	ACTATAGGGAGACCCATGGCGGCGGCCGGCCGG
MuTMEMR	GTCCATGGTAAGCTTAGTCCTGGCTGGCTGAGTTGC
PcDNAF	AAGCTTACCATGGACTACAAGGACG
PcDNAR	GGGTCTCCCTATAGTGAGTCG

The PCR product used generated *rav2Δ* was amplified with oligonucleotides RAV2URA3F and RAV2URA3R using pRS316 as a template; the PCR product was designed to give a clean deletion of the *RAV2* ORF. Cells were transformed, and colonies were selected on SD-URA media. The oligonucleotides YDR1-1 and URA-int were used to confirm rav2 deletion. ROGDI was integrated at the *RAV2* locus by transformation of the *rav2Δ::URA3* strain with a PCR product amplified from pCMV-SPORT6-ROGDI (Horizon Discovery) using oligonucleotides Rav2-RogdiFnew and Rav2-Rogdi Rev. Colonies were selected on supplemented minimal medium containing 5-fluoro-orotic acid to select against the colonies retaining the *URA3* gene (62). Yeast codon-optimized ROGDI (RecHu ROGDI) was PCR amplified from pUC57-containing codon-optimized ROGDI (Genscript) using oligonucleotides Rav2-RogdirecodeF and RogdirecodeR. The product was then transformed into *rav2Δ::URA3 cells*, and transformants were selected on medium containing 5-fluoro-orotic acid as described previously. Integration was confirmed by PCR with oligonucleotides YDR1-1 and rav2c4.

The strong yeast TEF promoter placed upstream of ROGDI in *TEF-rav2Δ*::RecHuROGDI strain was constructed by amplification of a rav2-Rogdi-TEF construct using Rav2-S1, S4-Rogdi-V3, and pYM-N19 as a template (63). The TEF construct was transformed into *rav2Δ*::yeROGDI and transformants selected on YEPD (yeast extract–peptone–dextrose) medium containing 100 μg/ml clonNAT. Genotype was confirmed using RogdirecodeintR and YDR1-1. The *rav1-Δ::KanMX* allele was amplified from genomic DNA of the BY4741 *rav1Δ::KanMX* strain (64) using oligonucleotides YJR1-7 and YJR6-12. The product was then transformed into the strain created previously, and colonies were selected on YEPD medium containing 200 μg/ml G418. Genotype was confirmed by PCR as described previously.

Rav⁻ phenotyping

Cells were grown until log phase, and a volume equivalent to 1 absorbance unit at 600 nm/ml was pelleted. Cells were washed and resuspended in 1 ml of YEPD. Serial fivefold dilutions of the cell suspensions were made in a 96-well plate, and cells were pinned, using a 48 spoke inoculating manifold, to YEPD buffered to pH 5 and YEPD containing 4 mM $ZnCl_2$. Plates were placed in a 37 °C incubator and imaged daily following 2 days of growth.

Yeast two-hybrid assay

Two-hybrid assays were performed as described by James *et al.* (38). In this system, the Gal4 DNA-binding domain is encoded in pAS2 and activating domain is encoded in pACT2 (65). The genes *HIS3* and *ADE2* in yeast strains PJ69-4a and PJ69-4α (Table 2) are under the control of the *GAL1* and

GAL2 promoters, respectively. Genes for proteins of interest are subcloned into the plasmid so that they result in a fusion protein with the corresponding GAL4 component. ROGDI was cloned into pAS2 with RogdipAS2F and RogdipAS2R and into pACT2 with RogdipAS2 and RogdipACT2R using a megaprimer cloning method (66). WDR7 (1–596) was cloned into pACT2 with WDR7 1F and WDR7pAS2 596R. DMXL2 1-625 was cloned into pAS2 with Rbcn3a 1-625F and Rbcn3a 1-625R. Both primers were constructed using megaprimer-based cloning. WDR72 was cloned into pACT2 using WDR721-589pACT2rev and WDR721-589pACT2R using In-Fusion Snap Assembly cloning (Takara). pACT2 plasmids were transformed into PJ69-4α and selected on SD lacking tryptophan. pAS2 plasmids were transformed into PJ69-4a and selected on SD medium lacking leucine. Empty pACT2 vector was used as a negative control for pACT2 plasmids, and pAS1-Lamin was used for pAS2 plasmids. Transformed cells were mated in YEPD, then transferred to SD medium lacking tryptophan and leucine media to select for diploids with both plasmids. Cells were resuspended in SD-Trp, Leu at 1 absorbance/ml, and one-fifth serial dilutions were performed. Cells were inoculated onto SD-Trp, Leu, Ade, His and SD-Trp, Leu, and Ade plates as described previously using an inoculation manifold. They were placed in a 30 °C incubator, and growth was imaged at 6 days postinoculation.

Crosslinking and immunoprecipitation

Mouse 4T1 breast cancer cells (American Type Culture Collection, CRL-2539) were grown in T75 flasks using Dulbecco's modified Eagle's medium containing 10% fetal bovine serum. For each immunoprecipitation (including the specific antibody and negative control of isotype-specific antibody), two T75 flasks grown to greater than 80% confluency were lysed in PBS lysis buffer (PBS, 0.5% NP-40, and protease inhibitors [PMSF, leupeptin, aprotinin, pepstatin, shymostatin]) and lysates were pooled. Lysate was rocked at 4 °C for 20 min to complete lysis, then insoluble material was pelleted by centrifugation at 6000*g* for 10 min. The supernatant was brought to 1.2 ml total volume using PBS lysis buffer. Crosslinking was done by adding dithiobis(succinimidylpropionate) to a final concentration of 0.5 mM and rocking the mixture at 4 °C for 30 min. After 30 min, the remaining dithiobis(succinimidylpropionate) was quenched by the addition of 1 M Tris–HCl (pH 7.4) to a final concentration of 50 mM and incubation at 4 °C for 15 min. Following quenching, 10% of the total lysate was set aside as an input sample. Prior to incubation with lysate, antibody was bound to protein-A Dynabeads (ThermoFisher Scientific; 10001D) according to the manufacturer's instructions. For the anti-DMXL1 antibody, 4 μg of total antibody was added. An equivalent amount of nonspecific rabbit immunoglobulin G (IgG) was used as a control. Lysate and antibody-bound beads were incubated on a rocker at 4 °C for 4 h. Beads were then removed from lysate using a magnetic stand and washed with PBS lysis buffer with protease inhibitors according to the manufacturer's instructions. Protein was eluted from beads by denaturing at 98 °C with cracking buffer (8 M urea, 5% SDS, 50 mM Tris–HCl [pH 6.8], and 5% β-mercaptoethanol). Samples were run on a 4 to 15% gradient SDS-PAGE gel (Bio-Rad) and transferred onto a polyvinylidene difluoride membrane using a Bio-Rad Transblot Turbo. Blots were blocked in 5% milk in Tris-buffered saline containing 0.1% Tween-20. Primary antibody was diluted in blocking buffer for 1.5 h at room temperature or overnight on a rocker. Blots were washed three times for 5 min each with Tris-buffered saline containing 0.1% Tween-20. Clean-blot IP Detection Reagent (HRP conjugate; 21230, ThermoFisher Scientific) was used (in place of an IgG secondary antibody) at a concentration of 1:500 in blocking buffer and incubated at room temperature for 1 h. Bio-Rad Clarity Max ECL (1705062) substrate and an Azure Sapphire Biomolecular Imager were used to visualize the blots. The data shown are representative of three biological replicates.

Immunofluorescence microscopy

Coverslips were washed with ethanol and water and coated with human collagen 4 at a concentration of 50 μg/ml for 30 min and then UV sterilized. Coverslips were placed in a 24-well plate, and 30,000 4T1 cells were seeded and allowed to grow overnight. The following day cells were washed with PBS and fixed with 4% formaldehyde in PBS for 10 min followed by permeabilization with 0.1% Triton X-100 for 10 min. Cells were labeled with LysoTracker Red DND-99 by incubating cells in fresh media containing 50 μM LysoTracker Red DND-99 for 30 min immediately prior to fixation.

For immunofluorescence, coverslips were incubated in blocking buffer (1% bovine serum albumin, 22.5 mg/ml glycine, and 0.1% Tween-20 in PBS) for 1 h. For indirect immunofluorescence detection of LAMP2, blocked coverslips were incubated in primary antibody (Anti-LAMP2 diluted to 1:100 in blocking buffer) for 1 h. Secondary antibody, anti-Rat-AlexaFluor 647 (Cell Signaling; catalog no.: 4418) was added at a concentration of 1:1000 and incubated for 1 h. Coverslips were washed three times for 5 min following secondary antibody incubation. For other immunofluorescence experiments, primary antibodies against DMXL1, ROGDI, and V_1A (Abcam; ab199326) antibodies were directly labeled with FlexAble IgG labeling kits from Proteintech (CoraLite Plus 488 [KFA001] or CoraLite Plus 647 [KFA003] as indicated) using the manufacturer's instructions. The labeled antibodies were combined in a total volume of 100 μl of blocking buffer before adding to the coverslip. Anti-ROGDI (Abcam; ab184954) was diluted to 1:100. Anti-DMXL1 (Novus; NBP1-90998) was diluted to 1:50; this antibody was recently validated for immunofluorescence in a mouse DMXL1 knockdown (41). Coverslips were washed three times for 5 min each after labeled primary antibody incubation. Slides were mounted onto the glass coverslips using ProLong Glass with NucBlue (Invitrogen; P36983) and then cured for 24 h before imaging.

Imaging of ROGDI and V_1A was done on a Zeiss AxioImager Z1 widefield fluorescence microscope equipped with a Hamamatsu ORCA-ER CCD camera using a 100×, 1.4 numerical aperture objective and GFP and Texas Red filter sets.

ROGDI/DMXL1, ROGDI/LAMP2, and DMXL1/LAMP2 images were captured with a Nikon Ti2-E SoRa spinning disk confocal microscope with a 60×, 1.4 numerical aperture oil immersion objective and the microscope operating in 2.8× SoRa mode. CoraLite 488- and 647-labeled antibodies were visualized with the corresponding filter sets; 4′,6-diamidino-2-phenylindole was visualized with 405 nm filter set. Stacks of images were captured with a step size of 0.3 μm; single slice images were chosen from near the middle of each stack. The images shown are representative of images from three separate biological replicates.

Images were analyzed using FIJI (67). For wide-field images, images from doubly labeled samples were synchronized, lines were drawn at the same position in each micrograph, and fluorescence intensities along each line were determined. For confocal images, colocalization was determined on grayscale images using the Coloc2 plugin, applied to either for the indicated region of interest (Fig. 6*A*) or the entire image shown (Figs. 6*B* and S1*A*). Pearson's *R* values with no threshold are shown. In all cases, the ratio of the randomized Pearson's/actual Pearson's value was 0.0.

LysoIP

In order to collect a lysosomal fraction from cells, we employed an adapted LysoIP protocol (46). Mouse lysosomal protein TMEM192 (Horizon Discovery; catalog no.: 3708193) was subcloned into pcDNA3 FLAG-HA (Addgene; #10792) using muTMEMF, muTEMEMR, pCDNAF, and pcDNAR to create a TMEM192-FLAG-HA fusion protein. This plasmid was transfected into 4T1 cells using Lipofectamine 3000 (catalog no.: L3000150; Thermo Fisher Scientific) at a cell density of 70%. Cells were grown for 24 h and then scraped in lysis buffer (150 mM NaCl, 50 mM Tris–HCl [pH 7.4], 5 mM EDTA, and 6% Optiprep) with protease inhibitors (PMSF, leupeptin, aprotinin, pepstatin, and chymostatin). Cells were lysed by passing through a 27-gauge needle five times. Cell debris and nuclei were pelleted by spinning at 1000*g* for 5 min at 4 °C. HA-Trap magnetic particles (25 μl; atd; Chromotek) for each immunoprecipitation were equilibrated in lysis buffer by washing twice using a magnet stand collect beads and allow removal of supernatant. The postnuclear supernatant was added to the HA-Trap magnetic particles and incubated on a rocker at 4 °C for 15 min. Magnetic particles were then separated using a magnet stand, supernatant was removed and set aside, and the magnetic particles were washed 2× with 200 μl lysis buffer. Protein bound to the magnetic particles was denatured in cracking buffer (8 M urea, 5% SDS, 50 mM Tris–HCl [pH 6], 1 mM EDTA, 5% β-mercaptoethanol, and 0.3% bromophenol blue) and analyzed by SDS-PAGE and immunoblotting. The experiment was repeated three times, and the blots shown are representative.

Subcellular fractionation

4T1 cells were grown in T75 flasks until they were at 70 to 80% confluency. Cells were washed in PBS and then scraped from dish in TBSE + protease inhibitors (150 mM NaCl, 50 mM Tris–HCl [pH 7.4], 5 mM EDTA with PMSF, leupeptin, aprotinin, pepstatin, and chymostatin). Cells were homogenized by passing thorough a 26-gauge needle 10 times. Cell debris and nuclei were pelleted by centrifugation at 700*g* for 5 min at 4 °C. Supernatant was transferred to a new 1.5 ml tube and centrifuged at 10,000*g* for 5 min to pellet mitochondria. Supernatant was then spun at 100,000*g* for 1 h in a Beckman-Coulter Optima XP ultracentrifuge to pellet the membrane fraction. Supernatant containing the cytosolic fraction was removed, and protein was precipitated with 10% trichloroacetic acid. The precipitated protein was solubilized in cracking buffer. The membrane pellet was also solubilized in cracking buffer. Samples were analyzed by SDS-PAGE followed by Western blotting as described previously. Blots shown are representative of three biological replicates.

Computational modeling

Predictive protein models were generated by AlphaFold2 and AlphaFold3 (47, 68). Analysis of the protein structures was done with USCF ChimeraX (69). AlphaFold3 models of individual proteins are assigned a pTM (predicted template modeling) score, and multiprotein complexes are assigned an ipTM (interface predicted template modeling) score (47). A pTM score >0.5 reflects a confident model likely to be similar to the true structure of the protein. An ipTM score between 0.6 and 0.8 represents low confidence in the relative position of proteins within a complex, whereas a score >0.8 reflect high confidence in the modeling of a complex. Both pTM and ipTM reflect more confident models as scores approach 1.

Data availability

Source data are available at 10.58120/upstate.26799115.

Supporting information—This article contains supporting information (reference pertaining to Fig. S1 (46); reference pertaining to Fig. S2 (47)).

Acknowledgments—We thank Dr Michael Jaskolka for initial recognition of structural similarity between Rav2 and ROGDI and for construction to DMXL2 two-hybrid constructs, Dr Farzana Tuli for construction of WDR7 two-hybrid constructs, and Dr Subhrajit Banerjee for assistance with LysoIP protocols. Figures were prepared using BioRender.

Author contributions—S. R. W. and P. M. K. conceptualization; S. R. W. methodology; S. R. W. validation; S. R. W. and P. M. K. formal analysis; S. R. W. investigation; P. M. K. resources; S. R. W. and P. M. K. data curation; S. R. W. writing–original draft; S. R. W. and P. M. K. writing–review & editing; P. M. K. supervision; P. M. K. project administration; P. M. K funding acquisition.

Funding and additional information—This work was funded by the National Institutes of Health R35 GM145256 (to P. M. K.). The content is solely the responsibility of the authors and does not necessarily represent the official views of the National Institutes of Health.

Conflict of interest—The authors declare that they have no conflicts of interest with the contents of this article.

Abbreviations—The abbreviations used are: cDNA, complementary DNA; DRTA, distal renal tubule acidosis; HA, hemagglutinin; HRP, horseradish peroxidase; IgG, immunoglobulin G; ipTM, interface predicted template modeling; KTS, Kohlschutter–Tonz syndrome; LAMP2, lysosome-associated membrane protein 2; LysoIP, lysosomal immunoprecipitation; NT, N-terminal; pTM, predicted template modeling; YEPD, yeast extract–peptone–dextrose.

References

1. Nelson, H., and Nelson, N. (1990) Disruption of genes encoding subunits of yeast vacuolar H (+)-ATPase causes conditional lethality. *Proc. Natl. Acad. Sci. U. S. A.* **87**, 3503–3507
2. Inoue, H., Noumi, T., Nagata, M., Murakami, H., and Kanazawa, H. (1999) Targeted disruption of the gene encoding the proteolipid subunit of mouse vacuolar H+-ATPase leads to early embryonic lethality. *Biochimica et Biophys. Acta Bioenerget.* **1413**, 130–138
3. Santos-Pereira, C., Rodrigues, L. R., and Côrte-Real, M. (2021) Emerging insights on the role of V-ATPase in human diseases: therapeutic challenges and opportunities. *Med. Res. Rev.* **41**, 1927–1964
4. Kawasaki-Nishi, S., Nishi, T., and Forgac, M. (2001) Yeast V-ATPase complexes containing different isoforms of the 100-kDa a-subunit differ in coupling efficiency and *in vivo* dissociation. *J. Biol. Chem.* **276**, 17941–17948
5. Banerjee, S., Clapp, K., Tarsio, M., and Kane, P. M. (2019) Interaction of the late endo-lysosomal lipid PI (3, 5) P2 with the Vph1 isoform of yeast V-ATPase increases its activity and cellular stress tolerance. *J. Biol. Chem.* **294**, 9161–9171
6. Kane, P. M. (1995) Disassembly and reassembly of the yeast vacuolar H+-ATPase *in vivo*. *J. Biol. Chem.* **270**, 17025–17032
7. Parra, K. J., Keenan, K. L., and Kane, P. M. (2000) The H subunit (Vma13p) of the yeast V-ATPase inhibits the ATPase activity of cytosolic V1 complexes. *J. Biol. Chem.* **275**, 21761–21767
8. McGuire, C. M., and Forgac, M. (2018) Glucose starvation increases V-ATPase assembly and activity in mammalian cells through AMP kinase and phosphatidylinositide 3-kinase/Akt signaling. *J. Biol. Chem.* **293**, 9113–9123
9. Nakamura, S. (2004) Glucose activates H+-ATPase in kidney epithelial cells. *Am. J. Physiol. Cell Physiol.* **287**, C97–C105
10. Zoncu, R., Bar-Peled, L., Efeyan, A., Wang, S., Sancak, Y., and Sabatini, D. M. (2011) mTORC1 senses lysosomal amino acids through an inside-out mechanism that requires the vacuolar H+-ATPase. *Science* **334**, 678–683
11. Bodzęta, A., Kahms, M., and Klingauf, J. (2017) The presynaptic v-ATPase reversibly disassembles and thereby modulates exocytosis but is not part of the fusion machinery. *Cell Rep.* **20**, 1348–1359
12. Smardon, A. M., Tarsio, M., and Kane, P. M. (2002) The RAVE complex is essential for stable assembly of the yeast V-ATPase. *J. Biol. Chem.* **277**, 13831–13839
13. Seol, J. H., Shevchenko, A., Shevchenko, A., and Deshaies, R. J. (2001) Skp1 forms multiple protein complexes, including RAVE, a regulator of V-ATPase assembly. *Nat. Cell Biol.* **3**, 384–391
14. Smardon, A. M., Nasab, N. D., Tarsio, M., Diakov, T. T., and Kane, P. M. (2015) Molecular interactions and cellular itinerary of the yeast RAVE (regulator of the H+-ATPase of vacuolar and endosomal membranes) complex. *J. Biol. Chem.* **290**, 27511–27523
15. Wang, H., Tarsio, M., Kane, P. M., and Rubinstein, J. L. (2024) Structure of yeast RAVE bound to a partial V(1) complex. *Proc. Natl. Acad. Sci. U. S. A.* **121**, e2414511121
16. Jaskolka, M. C., Tarsio, M., Smardon, A. M., Khan, M. M., and Kane, P. M. (2021) Defining steps in RAVE-catalyzed V-ATPase assembly using purified RAVE and V-ATPase subcomplexes. *J. Biol. Chem.* **296**, 100703
17. Sautin, Y. Y., Lu, M., Gaugler, A., Zhang, L., and Gluck, S. L. (2005) Phosphatidylinositol 3-kinase-mediated effects of glucose on vacuolar H+-ATPase assembly, translocation, and acidification of intracellular compartments in renal epithelial cells. *Mol. Cell Biol.* **25**, 575–589
18. Collins, M. P., and Forgac, M. (2020) Regulation and function of V-ATPases in physiology and disease. *Biochim. Biophys. Acta Biomembranes* **1862**, 183341
19. Einhorn, Z., Trapani, J. G., Liu, Q., and Nicolson, T. (2012) Rabconnectin3α promotes stable activity of the H+ pump on synaptic vesicles in hair cells. *J. Neurosci.* **32**, 11144–11156
20. Sethi, N., Yan, Y., Quek, D., Schupbach, T., and Kang, Y. (2010) Rabconnectin-3 is a functional regulator of mammalian Notch signaling. *J. Biol. Chem.* **285**, 34757–34764
21. Tuttle, A. M., Hoffman, T. L., and Schilling, T. F. (2014) Rabconnectin-3a regulates vesicle endocytosis and canonical Wnt signaling in zebrafish neural crest migration. *PLoS Biol.* **12**
22. Ratto, E., Chowdhury, S. R., Siefert, N. S., Schneider, M., Wittmann, M., Helm, D., *et al.* (2022) Direct control of lysosomal catabolic activity by mTORC1 through regulation of V-ATPase assembly. *Nat. Commun.* **13**, 4848
23. Kawabe, H., Sakisaka, T., Yasumi, M., Shingai, T., Izumi, G., Nagano, F., *et al.* (2003) A novel rabconnectin-3-binding protein that directly binds a GDP/GTP exchange protein for Rab3A small G protein implicated in Ca2+-dependent exocytosis of neurotransmitter. *Genes Cells* **8**, 537–546
24. Nagano, F., Kawabe, H., Nakanishi, H., Shinohara, M., Deguchi-Tawarada, M., Takeuchi, M., *et al.* (2002) Rabconnectin-3, a novel protein that binds both GDP/GTP exchange protein and GTPase-activating protein for Rab3 small G protein family. *J. Biol. Chem.* **277**, 9629–9632
25. Uhlén, M., Fagerberg, L., Hallström, B. M., Lindskog, C., Oksvold, P., Mardinoglu, A., *et al.* (2015) Tissue-based map of the human proteome. *Science* **347**, 1260419
26. Jaskolka, M. C., Winkley, S. R., and Kane, P. M. (2021) RAVE and rabconnectin-3 complexes as signal dependent regulators of organelle acidification. *Front. Cell Dev. Biol.* **9**, 698190
27. Schossig, A., Wolf, N. I., Kapferer, I., Kohlschütter, A., and Zschocke, J. (2012) Epileptic encephalopathy and amelogenesis imperfecta: Kohlschütter–Tönz syndrome. *Eur. J. Med. Genet.* **55**, 319–322
28. Schossig, A., Wolf, N. I., Fischer, C., Fischer, M., Stocker, G., Pabinger, S., *et al.* (2012) Mutations in ROGDI cause Kohlschütter-Tönz syndrome. *Am. J. Hum. Genet.* **90**, 701–707
29. Kelley, L. A., Mezulis, S., Yates, C. M., Wass, M. N., and Sternberg, M. J. E. (2015) The Phyre2 web portal for protein modeling, prediction and analysis. *Nat. Protoc.* **10**, 845–858
30. Lee, H., Jeong, H., Choe, J., Jun, Y., Lim, C., and Lee, C. (2017) The crystal structure of human Rogdi provides insight into the causes of Kohlschutter-Tönz Syndrome. *Sci. Rep.* **7**, 3972
31. Merkulova, M., Păunescu, T. G., Azroyan, A., Marshansky, V., Breton, S., and Brown, D. (2015) Mapping the H+(V)-ATPase interactome: identification of proteins involved in trafficking, folding, assembly and phosphorylation. *Sci. Rep.* **5**, 14827
32. Coupland, C. E., Karimi, R., Bueler, S. A., Liang, Y., Courbon, G. M., Di Trani, J. M., *et al.* (2024) High-resolution electron cryomicroscopy of V-ATPase in native synaptic vesicles. *Science* **385**, 168–174
33. Jimenez-Armijo, A., Morkmued, S., Ahumada, J. T., Kharouf, N., de Feraudy, Y., Gogl, G., *et al.* (2024) The Rogdi knockout mouse is a model for Kohlschütter–Tönz syndrome. *Scientific Rep.* **14**, 445
34. Rice, P., Longden, I., and Bleasby, A. (2000) EMBOSS: the European molecular biology open software suite. *Trends Genet.* **16**, 276–277
35. Jumper, J., Evans, R., Pritzel, A., Green, T., Figurnov, M., Ronneberger, O., *et al.* (2021) Highly accurate protein structure prediction with AlphaFold. *Nature* **596**, 583–589
36. Smardon, A. M., Diab, H. I., Tarsio, M., Diakov, T. T., Nasab, N. D., West, R. W., *et al.* (2014) The RAVE complex is an isoform-specific V-ATPase assembly factor in yeast. *Mol. Biol. Cell* **25**, 356–367
37. [preprint] Wang, H., Tarsio, M., Kane, P. M., and Rubinstein, J. L. (2024) Structure of yeast RAVE bound to a partial V1 complex. *bioRxiv*. https://doi.org/10.1101/2024.07.18.604153
38. James, P., Halladay, J., and Craig, E. A. (1996) Genomic libraries and a host strain designed for highly efficient two-hybrid selection in yeast. *Genetics* **144**, 1425–1436

39. [preprint] Evans, R., O'Neill, M., Pritzel, A., Antropova, N., Senior, A., Green, T., *et al.* (2022) Protein complex prediction with AlphaFold-multimer. *bioRxiv*. https://doi.org/10.1101/2021.10.04.463034
40. McGuire, C. M., Collins, M. P., Sun-Wada, G., Wada, Y., and Forgac, M. (2019) Isoform-specific gene disruptions reveal a role for the V-ATPase subunit a4 isoform in the invasiveness of 4T1-12B breast cancer cells. *J. Biol. Chem.* **294**, 11248–11258
41. Eaton, A. F., Danielson, E. C., Capen, D., Merkulova, M., and Brown, D. (2024) Dmxl1 is an essential mammalian gene that is required for V-ATPase assembly and function *in vivo*. *Function (Oxf)* **5**. https://doi.org/10.1093/function/zqae025
42. Parra, K. J., and Kane, P. M. (1998) Reversible association between the V1and V0 domains of yeast vacuolar H+-ATPase is an unconventional glucose-induced effect. *Mol. Cell Biol.* **18**, 7064–7074
43. Johnson, D. E., Ostrowski, P., Jaumouillé, V., and Grinstein, S. (2016) The position of lysosomes within the cell determines their luminal pH. *J. Cell Biol.* **212**, 677–692
44. Ebner, M., Puchkov, D., López-Ortega, O., Muthukottiappan, P., Su, Y., Schmied, C., *et al.* (2023) Nutrient-regulated control of lysosome function by signaling lipid conversion. *Cell* **186**, 5328–5346.e5326
45. Lemieux, B., Percival, M. D., and Falgueyret, J.-P. (2004) Quantitation of the lysosomotropic character of cationic amphiphilic drugs using the fluorescent basic amine Red DND-99. *Anal. Biochem.* **327**, 247–251
46. Abu-Remaileh, M., Wyant, G. A., Kim, C., Laqtom, N. N., Abbasi, M., Chan, S. H., *et al.* (2017) Lysosomal metabolomics reveals V-ATPase-and mTOR-dependent regulation of amino acid efflux from lysosomes. *Science* **358**, 807–813
47. Abramson, J., Adler, J., Dunger, J., Evans, R., Green, T., Pritzel, A., *et al.* (2024) Accurate structure prediction of biomolecular interactions with AlphaFold 3. *Nature* **630**, 493–500
48. Gandini, M. A., Souza, I. A., Fan, J., Li, K., Wang, D., and Zamponi, G. W. (2019) Interactions of rabconnectin-3 with Cav2 calcium channels. *Mol. Brain* **12**, 62
49. Dittrich, A., Ramesh, G., Jung, M., and Schmitz, F. (2023) Rabconnectin-3α/DMXL2 is locally enriched at the synaptic ribbon of rod photoreceptor synapses. *Cells* **12**, 1665
50. Crummy, E., Mani, M., Thellman, J. C., and Martin, T. F. (2019) The priming factor CAPS1 regulates dense-core vesicle acidification by interacting with rabconnectin3β/WDR7 in neuroendocrine cells. *J. Biol. Chem.* **294**, 9402–9415
51. Jaskolka, M. C., and Kane, P. M. (2020) Interaction between the yeast RAVE complex and Vph1-containing Vo sectors is a central glucose-sensitive interaction required for V-ATPase reassembly. *J. Biol. Chem.* **295**, 2259–2269
52. Collins, M. P., Stransky, L. A., and Forgac, M. (2020) AKT Ser/Thr kinase increases V-ATPase–dependent lysosomal acidification in response to amino acid starvation in mammalian cells. *J. Biol. Chem.* **RA120**, 013223
53. Sava, I., Davis, L. J., Gray, S. R., Bright, N. A., and Luzio, J. P. (2024) Reversible assembly and disassembly of V-ATPase during the lysosome regeneration cycle. *Mol. Biol. Cell* **35**, ar63
54. Liepina, L., Kalnina, M. L., Micule, I., Gailite, L., Rots, D., Kalnina, J., *et al.* (2021) Kohlschütter–Tönz syndrome: case report with novel feature and detailed review of features associated with ROGDI variants. *Am. J. Med. Genet. A* **188**, 1263–1279
55. Tata, B., Huijbregts, L., Jacquier, S., Csaba, Z., Genin, E., Meyer, V., *et al.* (2014) Haploinsufficiency of Dmxl2, encoding a synaptic protein, causes infertility associated with a loss of GnRH neurons in mouse. *PLoS Biol.* **12**, e1001952
56. Eaton, A. F., Danielson, E. C., Capen, D., Merkulova, M., and Brown, D. (2024) Dmxl1 is an essential mammalian gene that is required for V-ATPase assembly and function *in vivo*. *Function* **5**, zqae025
57. Stover, E., Borthwick, K., Bavalia, C., Eady, N., Fritz, D., Rungroj, N., *et al.* (2002) Novel ATP6V1B1 and ATP6V0A4 mutations in autosomal recessive distal renal tubular acidosis with new evidence for hearing loss. *J. Med. Genet.* **39**, 796–803
58. El-Sayed, W., Parry, D. A., Shore, R. C., Ahmed, M., Jafri, H., Rashid, Y., *et al.* (2009) Mutations in the beta propeller WDR72 cause autosomal-recessive hypomaturation amelogenesis imperfecta. *Am. J. Hum. Genet.* **85**, 699–705
59. Katsura, K., Horst, J., Chandra, D., Le, T., Nakano, Y., Zhang, Y., *et al.* (2014) WDR72 models of structure and function: a stage-specific regulator of enamel mineralization. *Matrix Biol.* **38**, 48–58
60. Rungroj, N., Nettuwakul, C., Sawasdee, N., Sangnual, S., Deejai, N., Misgar, R., *et al.* (2018) Distal renal tubular acidosis caused by tryptophan-aspartate repeat domain 72 (WDR72) mutations. *Clin. Genet.* **94**, 409–418
61. Gietz, D., St Jean, A., Woods, R. A., and Schiestl, R. H. (1992) Improved method for high efficiency transformation of intact yeast cell. *Nucleic Acids Res.* **20**, 1425
62. Boeke, J. D., La Croute, F., and Fink, G. R. (1984) A positive selection for mutants lacking orotidine-5′-phosphate decarboxylase activity in yeast: 5-fluoro-orotic acid resistance. *Mol. Gen. Genet.* **197**, 345–346
63. Janke, C., Magiera, M. M., Rathfelder, N., Taxis, C., Reber, S., Maekawa, H., *et al.* (2004) A versatile toolbox for PCR-based tagging of yeast genes: new fluorescent proteins, more markers and promoter substitution cassettes. *Yeast* **21**, 947–962
64. Winzeler, E. A., Shoemaker, D. D., Astromoff, A., Liang, H., Anderson, K., Andre, B., *et al.* (1999) Functional characterization of the S. cerevisiae genome by gene deletion and parallel analysis. *Science* **285**, 901–906
65. Bai, C., and Elledge, S. J. (1996) [27] Gene identification using the yeast two-hybrid system. *Methods Enzymol.* **273**, 331–347
66. Barik, S. (2002) Megaprimer PCR. *Methods Mol. Biol.* **192**, 189–196
67. Schindelin, J., Arganda-Carreras, I., Frise, E., Kaynig, V., Longair, M., Pietzsch, T., *et al.* (2012) Fiji: an open-source platform for biological-image analysis. *Nat. Methods* **9**, 676–682
68. Cramer, P. (2021) AlphaFold2 and the future of structural. *Biol. Nat. Struct. Mol. Biol.* **28**, 704–705
69. Meng, E. C., Goddard, T. D., Pettersen, E. F., Couch, G. S., Pearson, Z. J., Morris, J. H., *et al.* (2023) UCSF ChimeraX: tools for structure building and analysis. *Protein Sci.* **32**, e4792